J. Phys. D: Appl. Phys. **44** (2011) 375501 (8pp) doi:10.1088/0022-3727/44/37/375501

# Ag–Ti(C, N)-based coatings for biomedical applications: influence of silver content on the structural properties

**N K Manninen[1], R Escobar Galindo[2], N Benito[3], N M Figueiredo[4], A Cavaleiro[4], C Palacio[3] and S Carvalho[1]**

[1] Universidade do Minho, Dept. Física, Campus de Azurém, 4800-058 Guimarães, Portugal
[2] Instituto de Ciencia de Materiales de Madrid (ICMM -CSIC), Cantoblanco, 28049, Madrid, Spain
[3] Departamento de Física Aplicada (CXII), Universidad Autónoma de Madrid, Cantoblanco, 28049, Madrid, Spain
[4] SEG-CEMUC Mechanical Engineering Department, University of Coimbra, 3030-788 Coimbra

Received 15 April 2011, in final form 25 July 2011
Published 26 August 2011
Online at stacks.iop.org/JPhysD/44/375501

**Abstract**
Ag–TiCN coatings were deposited by dc reactive magnetron sputtering and their structural and morphological properties were evaluated. Compositional analysis showed the existence of Ag–TiCN coatings with different Ag/Ti atomic ratios (ranging from 0 to 1.49). The structural and morphological properties are well correlated with the evolution of Ag/Ti atomic ratio. For the samples with low Ag/Ti atomic ratio (below 0.20) the coatings crystallize in a B1-NaCl crystal structure typical of $TiC_{0.3}N_{0.7}$. The increase in Ag/Ti atomic ratio promoted the formation of Ag crystalline phases as well as amorphous $CN_x$ phases detected in both x-ray photoelectron spectroscopy and Raman spectroscopy analysis. Simultaneously to the formation of Ag crystalline phases and amorphous carbon-based phases, a decrease in $TiC_{0.3}N_{0.7}$ grain size was observed as well as the densification of coatings.

(Some figures in this article are in colour only in the electronic version)

## 1. Introduction

The increasing demand for sustainable products requires the development of new knowledge-based materials with advanced properties. These products are then expected to last longer, have better performance, be safe and be more efficient. These requirements, which maybe seen as a rule of thumb for most known materials, gain particular importance when dealing with applications involving the human body: the so-called biomaterials [1]. Fatigue fracture and wear have been identified as major problems associated with implant loosening, stress-shielding and ultimate implant failure. Also, medical devices sometimes have to be physically removed due to infection. In fact, these wear-related problems are being studied by the development of new functional biomaterials which can intend to have some improved physical, mechanical, tribological or biological properties [2–4]. The tendency in implant science is to replace the total hip prosthesis, which was usually made of a variety of materials such as metals, ceramics, polymers and composites, by those materials coated with protective thin films.

Different types of PVD hard ceramic coatings were frequently considered as possible solutions to overcome the drawbacks mentioned above. In recent years, nanocomposite protective films have gained popularity due to their superior mechanical and tribological properties compared with traditional single-phase films. Superhard nanocomposites based on the combination of various transition metal nitrides, carbides and carbonitrides have been reported in recent years [5–8]. Clearly controlling the nanoscale coating structure in order to achieve the best properties (enhanced hardness and tribological behaviour) is the main motivation of these papers. Titanium carbonitride (TiCN) presents excellent wear resistance, high hardness and good corrosion resistance beyond its non-cytotoxic character. These properties justify that TiCN could be a potential coating for hip implants. TiCN has been studied in the last few decades especially the structural properties and their relation to the mechanical and tribological behaviour, which determines the in-service performance in mechanical applications [3, 4, 9, 10]. As an example, Martínez-Martínez *et al* reported that in TiCN coatings deposited by magnetron sputtering, a C enrichment

 © 2011 IOP Publishing Ltd Printed in the UK & the USA

**Table 1.** Chemical composition, thickness, deposition rate of deposited samples and some experimental details.

| Series | Ag/Ti ratio | Chemical Composition (% at.) Ag | Ti | C | N | $\Phi N_2$ (sccm) | $\Phi C_2H_2$ (sccm) | Current Density (mA cm$^{-2}$) Ti | Ti + Ag | Thickness ($\mu$m) | Deposition Rate ($\mu$m/h) |
|---|---|---|---|---|---|---|---|---|---|---|---|
| 1st Series | 0 | 0 | 37 | 29 | 34 | 6 | 6 | 10 | 0 | 2.9 | 1.3 |
| | 0.06 | 2 | 35 | 30 | 33 | 6.35 | 6 | 10 | 1.25 | 2.0 | 1.6 |
| | 0.20 | 6 | 32 | 30 | 32 | 8.55 | 8 | 10 | 6 | 1.4 | 1.4 |
| 2nd Series | 0.40 | 11 | 27 | 31 | 31 | 9.5 | 8.5 | 10 | 4.5 | 3.0 | 1.8 |
| | 0.77 | 20 | 26 | 30 | 24 | 12 | 11 | 10 | 7.5 | 2.9 | 2.6 |
| | 1.49 | 27 | 18 | 33 | 22 | 6.5 | 5.5 | 5 | 5 | 3.2 | 1.4 |

led to the formation of an amorphous carbon phase that can help to decrease the friction coefficient and the wear rate, although promoting a hardness reduction, conditions giving the best performance in some applications, such as in hip implants [11].

Previous results obtained demonstrated that although these types of biomaterials presented good mechanical properties and low cytotoxicicty [3, 12] they were prone to be colonized by *Staphylococcus epidermidis*. Hence this strengthens the urgent need for improving coatings incorporating antimicrobial properties. The current investigations support that use of silver ion or metallic silver as well as silver nanoparticles can be exploited in medicine for burn treatment, dental materials, coating stainless steel materials, textile fabrics, water treatment, as well as sunscreen lotions, and these possess low toxicity to human cells [13, 14].

Indeed, several studies have been performed describing the use of silver for biomedical applications [15–17]. However, they only consider silver antimicrobial action, disregarding how silver is incorporated and/or its morphology. In fact, the antimicrobial property of silver is related to the amount of silver, and the rate of silver released is correlated with structural properties.

The aim of this study is the production and structural characterization of Ag–TiCN for hip implant applications and the focus is to study the influence of silver addition to the structure of TiCN coatings produced by dc reactive magnetron sputtering. According to the results obtained by several authors, the functional properties are strongly correlated with the coating structure. On the one hand the mechanical/tribological behaviours are clearly governed by the balance between crystalline and amorphous phases. On the other hand, silver antimicrobial properties are mainly controlled by the amount of silver present in the system and by the surface-to-volume ratio, which depends on the morphology of silver clusters. Thus, in order to understand the functional properties of Ag–TiCN the knowledge of structure and morphology is a prerequisite. In fact a deep investigation of the structure needs to be done first in order to understand the usually very complex results one obtains from tribological and biological tests. This work intends to contribute to this comprehension field.

## 2. Materials and methods

Ag–TiCN samples were deposited by reactive dc magnetron sputtering from a high-purity Ti target (200 × 100 mm$^2$) onto polished and ultrasonically cleaned 316 L stainless steel (20 × 20 mm$^2$) and single crystalline silicon (1 0 0). High-purity silver is incorporated on a second Ti target in the form of nuggets. Two series of samples were deposited using this Ti target with 6 and 14 Ag nuggets, resulting in relative Ag sputtering areas (only the preferential eroded zone of the target is considered) of 15% and 43%, respectively.

To further vary the Ag content in the films in both series the current density applied to each target was also changed. The substrates were previously sputter-etched for 20 min in an $Ar^+$ atmosphere. The depositions were carried out in Ar+$C_2H_2$+$N_2$ mixtures using an Alcatel SCM650 apparatus, with the substrates rotating at 70 mm over the target at a constant speed of 8 rpm. The base pressure in the deposition chamber was about $10^{-3}$ Pa and rose up to values between $3.1 \times 10^{-1}$ and $4.7 \times 10^{-1}$ Pa during the depositions. The films were grown at a constant temperature (573 K) and bias voltage (−70 V). Argon flow was kept constant at 60 sccm while the reactive gases fluxes ($C_2H_2$ and $N_2$) were changed as is indicated in table 1. The variation in the reactive gas fluxes was performed in order to maintain approximately constant the C and the N contents, although the density current applied to the targets was changed. The stoichiometry of the deposited films was investigated by a Cameca SX 50 electron probe microanalysis (EPMA) apparatus. Ball crater tests were used to measure the film thickness. The structure and phase distribution of the coatings were determined by x-ray diffraction (XRD) using a conventional Philips PW 1710 diffractometer, operating with Cu K$\alpha$ radiation in grazing incidence mode (angle of incidence of 1.5°).

The microstructure analysis was carried out on Tecnai G2 transmission electron microscope operated at 200 kV. The morphology of the coatings was evaluated by scanning electron microscopy (EDAX-Nova nanoSEM 200).

In order to analyse the chemical bonding Raman spectroscopy and x-ray photoelectron spectroscopy (XPS) were performed. Raman spectra were acquired with a Renishaw InVia Microscope. The excitation light was the 514.5 nm line of an Ar laser.

XPS spectra were acquired using a hemispherical analyser (SPECS EA-10 Plus).The pass energy was 15 eV giving a constant resolution of 0.9 eV. The Ag 3d5/2 line at 367.9 eV was used in order to calibrate the binding energies. A twin anode (Mg and Al) x-ray source was operated at a constant power of 300 W using Al K$\alpha$ radiation. The samples were sputter-cleaned *in situ* using a broad 3 keV$Ar^+$ beam for 10 min.

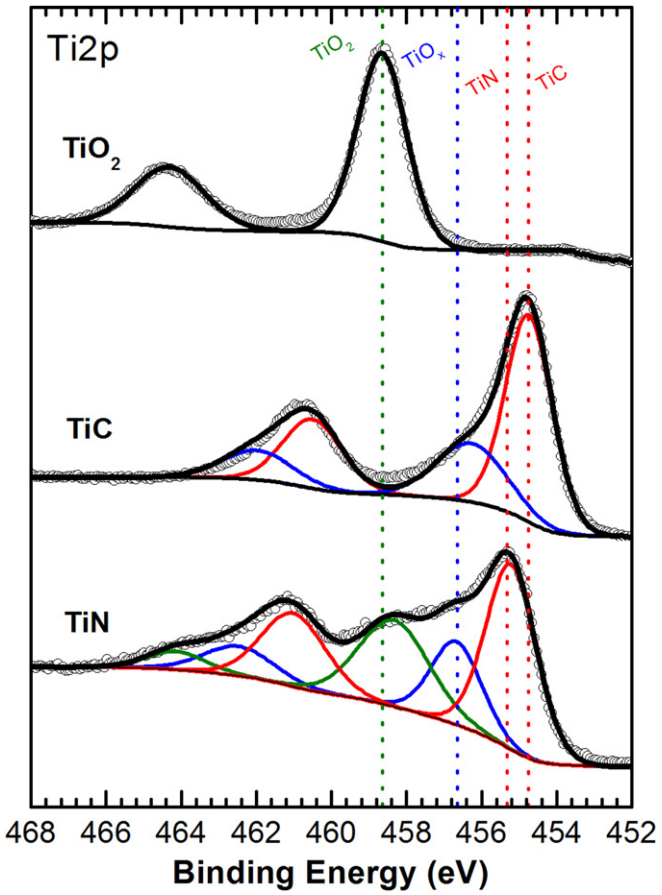


**Figure 1.** XPS spectra of Ti2p core level of TiN, TiC and $TiO_2$ reference samples.

Due to the large dispersion of reference peak values found in the literature, XPS analysis of TiN, TiC and $TiO_2$ reference samples was performed to obtain experimentally the binding energies of interest. In figure 1 the Ti2p spectra of the reference samples is presented clearly showing the doublets for TiC (454.6, 460.4 eV), TiN (455.4, 461.2 eV) and $TiO_2$ (458.5, 464.2 eV). In the TiN and TiC samples we have also found a doublet at (456.6, 462.3 eV) that some authors have associated with $Ti_2O_3$ [18]. We have labelled it here as $TiO_x$ as it might include other titanium oxidation states. It is worth noting that the separation of the Ti2p3/2 and Ti2p1/2 components for the oxide doublets is 5.7 eV, while for the nitride and carbide is 5.8 eV. This is in very good agreement with the theoretical values expected. In table 2 the binding energies of the C1s, N1s, Ti2p and O1s bands found for the reference samples are summarized and they will be used in the discussion of the XPS results.

## 3. Results and discussion

### *3.1. Deposition rate and chemical composition*

The synthesis conditions together with the chemical composition and the thickness of the coatings are summarized in table 1. The film thicknesses ranged from 1.4 to 3.2 $\mu$m. The deposition rate tends to increase with the increment of $J_{Ti+Ag} + J_{Ti}$, as is clearly seen in figure 2. However, for

**Table 2.** The binding energies of the C1s, N1s, Ti2p and O1s bands found for the reference samples.

| Bond | Binding Energy (eV) | FWHM (eV) |
|---|---|---|
| C-Ti | $282.0 \pm 0.2$ | $1.3 \pm 0.1$ |
| C-C | $285.1 \pm 0.2$ | $1.7 \pm 0.3$ |
| C-O | $288.7 \pm 0.1$ | $2.0 \pm 0.1$ |
| C-N | $286.9 \pm 0.1$ | $1.2 \pm 0.3$ |
| N-Ti | $397.2 \pm 0.1$ | $1.5 \pm 0.2$ |
| N-C | $399.2 \pm 0.2$ | $2.2 \pm 0.1$ |
| Ti-C | $454.6 \pm 0.1$ | $1.4 \pm 0.1$ |
| | $460.4 \pm 0.1$ | $2.2 \pm 0.2$ |
| Ti-N | $455.4 \pm 0.1$ | $1.6 \pm 0.2$ |
| | $461.2 \pm 0.1$ | $1.8 \pm 0.2$ |
| Ti-Ox | $456.6 \pm 0.3$ | $1.8 \pm 0.3$ |
| | $462.3 \pm 0.3$ | $2.1 \pm 0.1$ |
| Ti-O2 | $458.5 \pm 0.2$ | $1.7 \pm 0.2$ |
| | $464.2 \pm 0.2$ | $2.1 \pm 0.1$ |
| O-Ti | $531.1 \pm 0.2$ | $2.4 \pm 0.1$ |
| O-C | $533.2 \pm 0.3$ | $2.0 \pm 0.1$ |

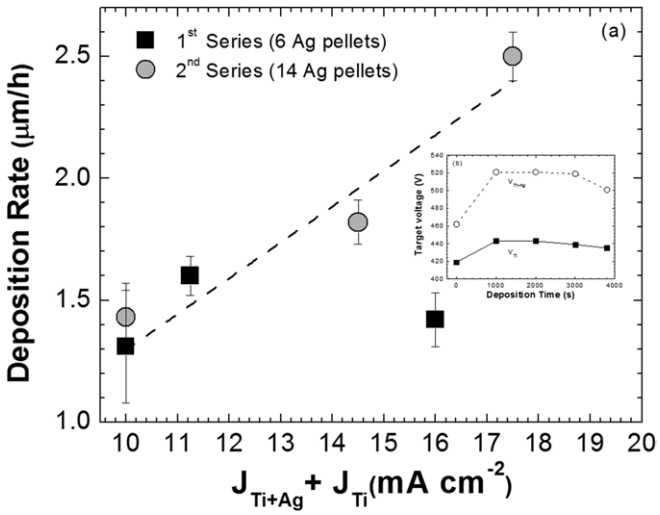


**Figure 2.** (*a*) Deposition rate for pure TiCN and Ag–TiCN coatings as function of $J_{TiAg} + J_{Ti}$ for first and second series. (*b*) Evolution of the potential on the targets $V_{TiAg}$ and $V_{Ti}$ as a function of $J_{TiAg} + J_{Ti}$ during the deposition of the sample processed with $J_{Ti+Ag} + J_{Ti} = 16\,mA\,cm^{-2}$.

the first series a poisoning effect is observed in the sample with the highest current density. This is probably due to the simultaneous increase in the flow of reactive gases with the current density. In the inset of figure 2, it is possible to observe the voltage increase in both targets during the deposition of the sample processed with $J_{Ti+Ag} + J_{Ti}$ of $16\,mA\,cm^{-2}$. The target voltage increase is due to the change of the target surface condition. In fact, due to the presence of reactive gases ($N_2 + C_2H_2$), both TiN and TiC layers should be formed at the Ti surface targets (phenomenon called the poisoning effect). Since the sputtering yield of both compounds is lower than that of Ti, a decrease in the deposition rate is consequently observed [19, 20]. Concerning the others depositions, no significant changes on the targets voltage values were observed during the deposition time.

Also, it is possible to observe that the increment on the target voltage is higher for the TiAg target than for the Ti

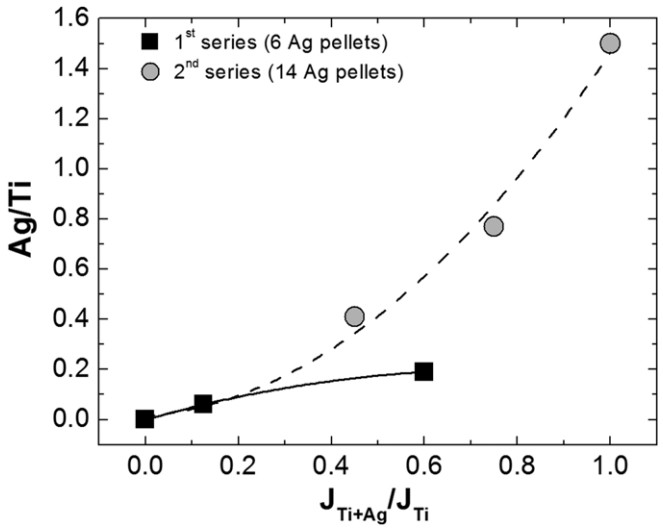


**Figure 3.** Ag/Ti atomic ratio versus $J_{TiAg}/J_{Ti}$ ratio for first and second series.

target. This effect cannot be explained from the formation of a silver nitride phase on the target surface, since silver is a poor nitride former. Depla *et al* justify the increment on the target voltage during sputtering of silver target in an $Ar/N_2$ plasma, by the presence on non-reacted N atoms in the target top surface layers [21].

The chemical composition of the samples deposited onto silicon, measured by EPMA, is also given in table 1. The compositional analysis shows that by increasing the $J_{TiAg}/J_{Ti}$ ratio for the first series the Ti content in the coatings decreased from 37 to 32 at% along with an increase in the Ag content from 0 to 6 at%. The C and N contents do not change significantly with the synthesis conditions. In the second series, the increase of Ag area promotes an increase in the silver contents in the coatings. The silver content changes from 11 to 27 at% while Ti content decreases from 27 to 18 at%. It can be seen that the current density applied to each magnetron ($J_{TiAg}$ and $J_{Ti}$) is the driven parameter for the film chemical composition. To that respect, figure 3 shows the variation of the Ag/Ti ratio versus $J_{TiAg}/J_{Ti}$ ratio. It is observed that in the second series, the raise in Ag/Ti ratio by increasing the current applied on Ti + Ag target is faster than in the first series. In the first series, this increase is lower due the smaller erosion area of Ag on Ti target. This means that it is not only the silver content that should control the properties of films but also the Ag/Ti atomic ratio.

### 3.2. Phase formation

XRD analysis was carried out in order to understand the evolution of the structure with the variation of Ag/Ti atomic ratio. The XRD patterns are shown in figure 4 and the main identified crystalline phases are depicted, namely $TiC_{0.3}N_{0.7}$ (ICDD card no 00-042-1488) and Ag (ICDD card no 00-004-0783). The differences in the chemical composition correlate well with the differences observed in the developed structure. In particular, for the sample without silver the films crystallize in a B1-NaCl crystal structure typical for $TiC_{0.3}N_{0.7}$ although

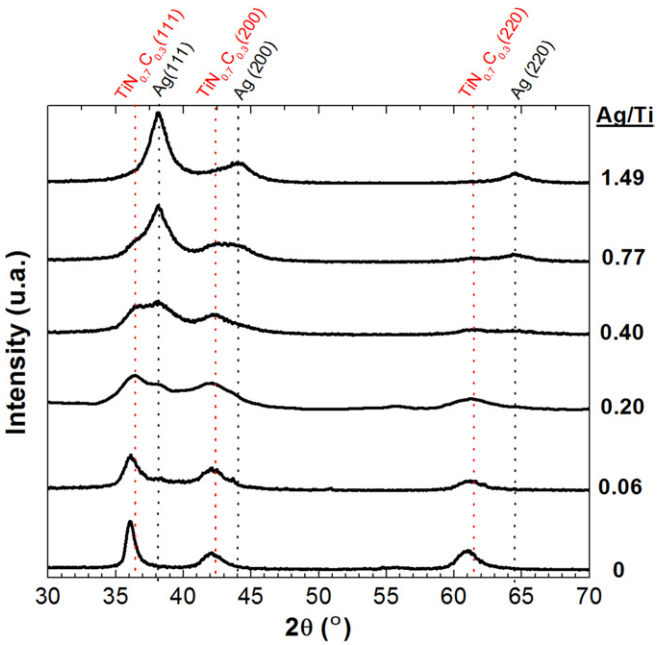


**Figure 4.** XRD patterns of the pure TiCN and Ag–TiCN coatings deposited by dc reactive magnetron sputtering, with different Ag/Ti atomic ratios.

a peak shift towards lower angles is denoted. This fact is in agreement with the measured chemical composition because these samples contain a slightly higher C/N atomic ratio than $TiC_{0.3}N_{0.7}$. Similar behaviour was observed for the samples with low Ag/Ti atomic ratio (0.06 and 0.20), although a new diffraction peak attributed to Ag (1 1 1) begins to appear.

The samples with Ag/Ti atomic ratio $\geqslant$0.40 also exhibit a polycrystalline structure, clearly with the formation of nanosized Ag clusters. For the Ag/Ti = 0.40 sample the structure is characterized by broader peaks in the range 35°–45°. It is difficult to unequivocally identify which phases are formed. However, in agreement for the samples with low Ag/Ti atomic ratio there are fcc phases that have the main peaks close to these values (TiCN and Ag). It is possible to infer that the XRD patterns reveal, at least, the development of a mixture of fcc-$TiC_{0.3}N_{0.7}$ (clearly visible for lowest Ag/Ti atomic ratio) and fcc-Ag crystalline phases (clearly visible for the highest Ag/Ti atomic ratio). In fact, by increasing the Ag/Ti atomic ratio, the fcc-Ag phase becomes predominant for the Ag/Ti atomic ratio of 0.77. The increment in the Ag/Ti ratio leads to a loss of the XRD peak intensity and crystal size of the TiCN phase. These changes can be understood due to the interruption of the growth of the TiCN phase by the nucleation of Ag nanocrystals and/or by the presence of an amorphous layer [22]. In fact, the low Ti/(C+N) ratio suggests the presence of an additional XRD amorphous phase, most likely of C or $CN_x$ type. Indeed, these phases were also observed within the TiCN and ZrCN systems [1, 3, 23]. The presence of this amorphous layer was confirmed by Raman spectroscopy and XPS analysis.

The XRD patterns of the Ag-containing films show, even for the lowest Ag contents, evidence for the presence of crystalline Ag. A small bump close to 38.12° (standard position of the (1 1 1) peak of fcc-Ag phase) can be detected

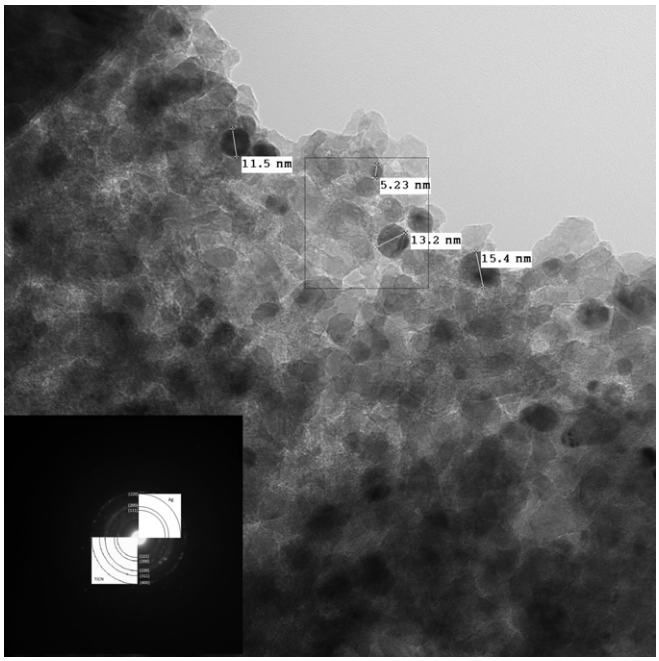


**Figure 5.** TEM micrograph from the cross-section of the Ag–TiCN coatings with Ag/Ti = 0.40 The inset shows the diffraction pattern from the selected area.

on the 0.06 Ag/Ti film, which becomes more and more evident with the Ag content increase until it gives rise to well defined and progressively narrower peaks. The grain size of TiCN and Ag phases was determined by the Scherrer formula taking, in both cases, the (1 1 1) peak. The calculated values varied from 15 down to 9 nm and from 5 up to 8 nm, for TiCN and Ag, respectively, with the increase in Ag/Ti. This variation should be due to the simultaneous growth of Ag, TiCN and amorphous phases. During the deposition of TiCN phase the addition of Ag and/or the presence of the C-amorphous layer cause an interrupted nucleation of the crystals, leading to smaller crystal sizes [22, 24]. However, due to the great mobility of Ag atoms, the increase in the Ag content progressively leads to higher Ag crystals, explaining the inverse trends of grain size for TiCN and Ag phases. In conclusion, the coatings should be imagined as a nanocomposite structure consisting of nanocrystals of both Ag and TiCN phases embedded in a C-rich amorphous matrix (incorporating N).

The nanocrystallinity of the Ag and TiCN grains can be confirmed by TEM cross- section observation. Figure 5 shows the TEM micrograph of the coating with Ag/Ti = 0.40. A closer look at the figure 5 reveals nanocrystallites with sizes ranging from 5 to 17 nm. In the inset of this figure, a selected diffraction (SAD) pattern is presented. SAD pattern also shows diffuse rings where discrete spots are superimposed, revealing, as it would be expected, a nanocrystalline structure. Two different phases, both with a fcc structure, were indexed. The first phase presents a lattice parameter ($a$ = 0.429 nm) very close to the $TiC_{0.3}N_{0.7}$ phase (whose stress-free lattice parameter is 0.426 nm) while the second pattern can be indexed to the Ag phase since the lattice parameter obtained by the SAD ($a$ = 0.408 nm) is close to this phase ($a$ = 0.409 nm, stress free). Meanwhile, the analysis of the Debye–Scherrer rings indicates growth on the (1 1 1), (2 0 0), (2 2 0), (3 1 1) and (4 0 0) planes that can be assigned with the TiCN phase and also growth on the (1 1 1), (2 0 0) and (2 2 0) planes for the Ag phase.

### *3.3. SEM analysis*

The morphology of the coatings is disclosed by cross-sectional SEM micrographs of fractured samples and it is shown in figure 6, for representative samples—Ag/Ti ratios of 0 (figure 6(*a*)); 0.20 (figure 6(*b*)); 0.40 (figure 6(*c*)) and 1.49 (figure 6(*d*)). The cross-section of the sample without silver (figure 6(*a*)) shows a columnar-type structure with high porosity. The low temperature during the film growth (573 K), associated with low bombardment conditions, promotes the development of this kind of structure due to the low adatom mobility. With the increase of a second crystalline phase (Ag) and the simultaneous growth of C(N)-based amorphous phases, the films became slightly less porous. For the sample with Ag/Ti of 0.40 (figure 6(*c*)) it is possible to see the presence of Ag nanoclusters in the boundaries of the columns near the coating surface, which was in some way predictable, once second phases usually tend to form in grain boundaries [22]. In the sample with Ag/Ti of 1.49 (figure 6(*d*)) it is possible to see silver clusters and some aggregates on the surface (the inset of figure 6(*d*)).

### *3.4. XPS and Raman spectroscopy*

Raman spectroscopy and XPS studies were performed on the Ag–TiCN samples, deposited on silicon substrates, with different Ag/Ti atomic ratios. XPS analysis was carried out with the aim of obtaining further information on the chemical bonding. Figure 7 shows the (*a*) Ti2p, (*b*) C1s, (*c*) N1s and (*d*) Ag3d core level XPS spectra of the deposited Ag–TiCN films with Ag/Ti atomic ratio of 0, 0.20, 0.40 and 1.49.

In figure 7(*a*), there are three doublets clearly identified in the Ti2p spectra of all samples. The first two doublets with Ti2p3/2 components centred at 458.5 eV and 456.6 eV, respectively, can be straightforwardly ascribed to $TiO_2$ and $TiO_x$ bonds for all samples as derived from the analysis of the reference samples (see figure 1 and table 2). The oxygen impurities exeunt due to residual oxygen in the vacuum chamber, in the targets and also due to contamination after deposition. For the sample without silver the third contribution is found to be at 455.1 eV (for the Ti2p3/2 component), that is in between the TiC (454.6 eV) and TiN (455.4 eV) bonds. This suggests the formation of a TiCN phase in good agreement with the XRD results previously shown. Similar behaviour is found for the sample with Ag/Ti = 0.20. However, as the silver ratio increases there is a slight but progressive shift of this third doublet towards higher binding energies. In the sample with Ag/Ti = 0.40 the third doublet is centred at 455.2 eV while for Ag/Ti = 1.49 it is at 455.4 eV, namely the binding energy of TiN. This shift is therefore ascribed to a continuous decrease of the titanium bonded to carbon. The Gibbs free energy for the formation of TiN phases is $-290\,\mathrm{kJ\,mol^{-1}}$ and for TiC is $-180\,\mathrm{kJ\,mol^{-1}}$ [25]. Therefore, with the decreasing of Ti content, there is a clear trend to the formation of the

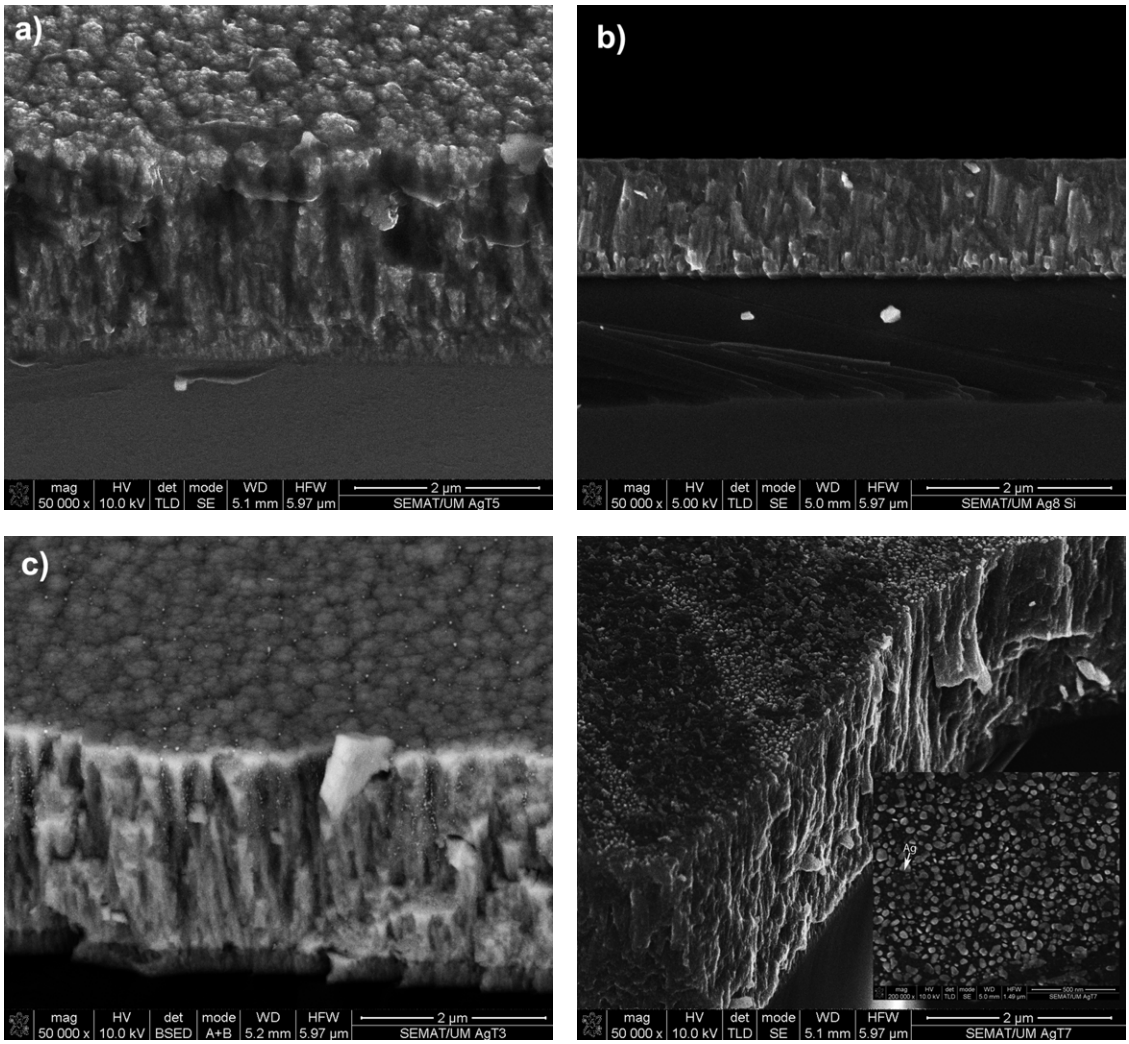


**Figure 6.** Cross-sectional SEM micrographs for different atomic ratios Ag/Ti: (*a*) 0 (*b*) 0.20 (*c*) 0.40 (*d*) 1.49. The inset of figure 6(*d*) shows the SEM image from the sample surface where Ag clusters are visible.

thermodynamically more stable nitride phases. In fact when analysing the C1s spectra in figure 7(*b*), the intensity of component ascribed to the C–Ti bonds at 282 eV decreases with the increase in the Ag/Ti ratio. In particular, for the sample with Ag/Ti = 1.49 this contribution simply disappears. On the other hand, for samples with high Ag/Ti ratio there is an increase in the intensity of the component ascribed to C–N bonds (286.9 eV), which is parallel to the behaviour of the component assigned to N–C bonds in the N1s spectra (see below), reinforcing the idea of the formation of an amorphous C-phase incorporating N. In the N1s spectra of figure 7(*c*), two contributions were found at 397.0 eV and 399.2 eV ascribed to N–Ti and N–C bonds, respectively (see table 1). The intensity of the N–C component becomes significant when the Ag/Ti increases (in agreement with the results for C1s spectra). Therefore, we can state that the presence of CN bonds is observed in the samples with Ag/Ti atomic ratios of 0.40 and 1.49 and the appearance of these bonds is attributed to the decrease in Ti content in the coatings. The excess of C and N (low Ti/C+N) ratio, as is possible to confirm by the composition results, promotes the formation of CN amorphous phases detected in both XPS and Raman spectroscopy analysis (see below). Finally, from the analysis of Ag 3d photoelectron spectra (figure 7(*d*)) it was possible to confirm that the only contribution is the Ag–Ag metal bonds, which was somehow predictable due to the low solubility of C and N in silver.

Figure 8 shows the Raman spectra of deposited Ag–TiCN samples with Ag/Ti atomic ratios 0, 0.20, 0.40 and 1.49. The aim of Raman spectroscopy analysis was to confirm the interpretation of structural and chemical bonding aspects done by XPS and XRD. As already discussed from the XRD analysis it is possible to observe the presence of broad peak between 35 and 45° for the sample with Ag/Ti atomic ratio of 0.20 and 0.40, which may be associated with the contribution of different nanocrystalline phases: TiCN and Ag, which presents three diffraction peaks between 36° and 38.6° (ICDD card nr. 21-1272). In the literature for TiN four peaks at approximately 225 (TA), 315 (LA), 450 (2A) and 550 $cm^{-1}$ (TO), and for TiC four peaks located at 280, 385, 585 and 675 $cm^{-1}$ are identified in the Raman spectra [1, 3, 26, 27]. According to our results (figure 8) it seems that the TiCN bonds should be located between TiN and TiC peaks.

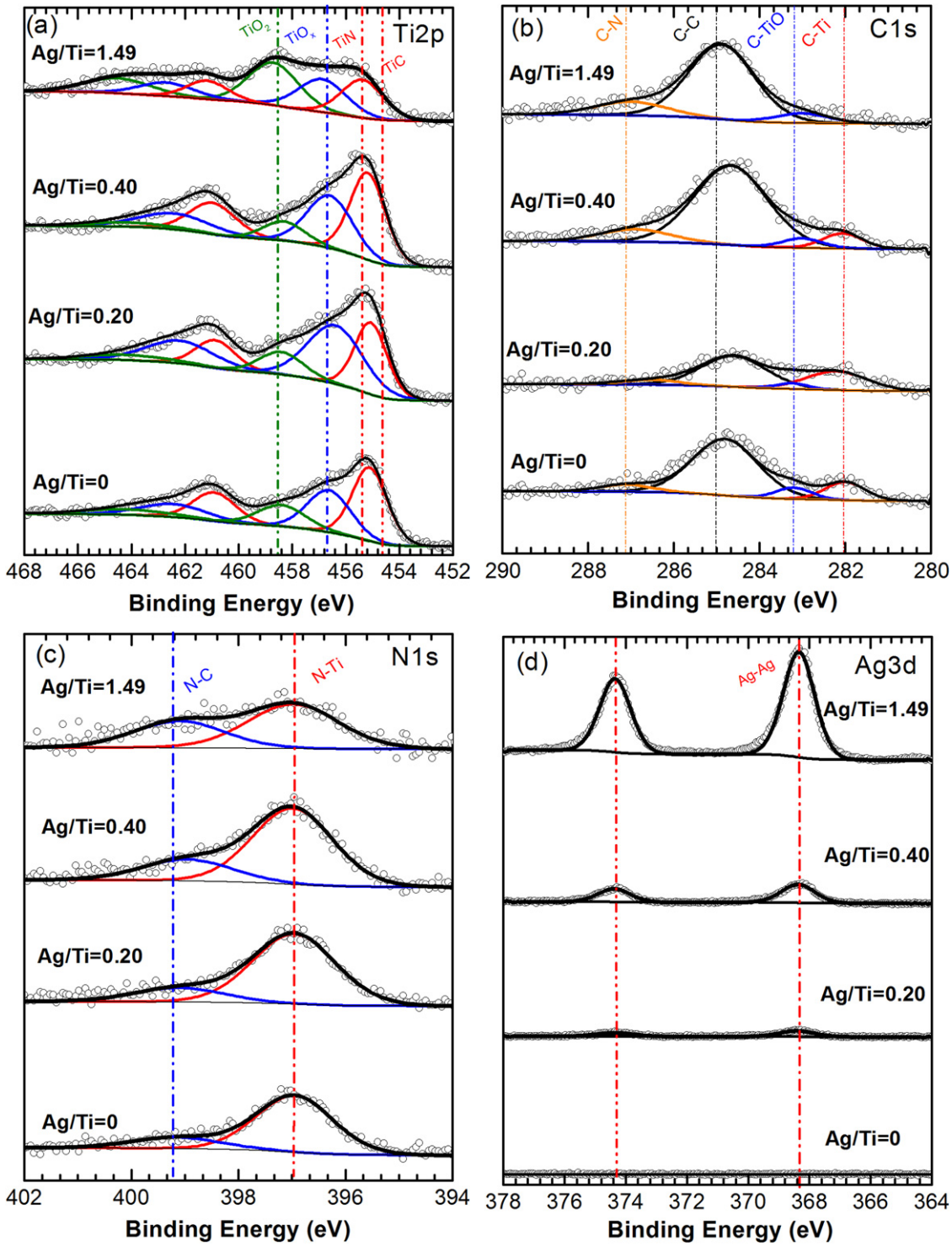


**Figure 7.** XPS spectra of (*a*) Ti2p, (*b*) C1s, (*c*) N1s and (*d*) Ag3d core levels of the Ag–TiCN coatings deposited by dc reactive magnetron sputtering with different Ag/Ti atomic ratios.

In the region between 1250 and 1595 $cm^{-1}$ several authors assigned carbon phases such as C-N at 1250 $cm^{-1}$ and C=N at 1500 $cm^{-1}$ as well as D and G bands of carbon materials at 1370 and 1580 $cm^{-1}$ [23, 28, 29]. Due to the similarity of the vibrational frequencies of C–C and C–N the interpretation of the results is difficult due to the appearance of broad bands. Nevertheless, the Raman band around 720 $cm^{-1}$, that starts to appear in the sample with Ag/Ti atomic ratio of 0.40, is also associated with the presence of C–N bonds [3], which allows confirming the presence of N in the amorphous CN phases as predicted from XPS results.

## 4. Conclusions

Ag–TiCN thin films were deposited by reactive magnetron sputtering with different density of currents applied to the Ti

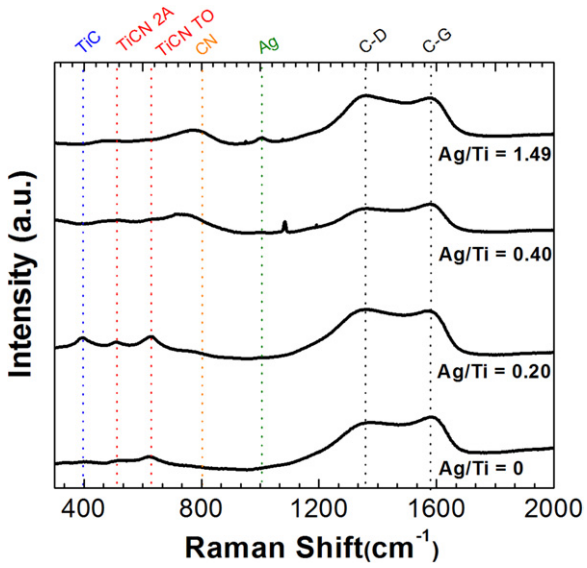


**Figure 8.** Raman spectra of the Ag–TiCN coatings for different Ag/Ti ratios.

and Ti+Ag targets, which controls the chemical composition of the samples studied. The structure evolution is correlated with the Ag/Ti atomic ratio. Samples with low Ag/Ti atomic ratio (<0.20) crystallized in a B1-NaCl crystal structure typical of $TiC_{0.3}N_{0.7}$. With the increase in Ag/Ti atomic ratio a second crystalline phase begins to appear promoting a reduction in the grain size and a densification of the coatings. In samples with intermediate Ag/Ti ratio (0.20 and 0.40) the increase in silver content promotes a competitive growth between Ag and $TiC_{0.3}N_{0.7}$ phases. Simultaneously, amorphous carbon-based phases begin to appear. Silver phases and CN tends to segregate in the grain boundaries of $TiC_{0.3}N_{0.7}$ causing a decrease in the grain size and a densification of the coatings. In samples with high Ag/Ti atomic ratio (>0.77), Ag appears as the dominant crystalline phase. According to the results obtained in the XPS analysis, the TiCN bonds are replaced by TiN bonds as a consequence of the decrease in Ti content with the increase in the Ag/Ti atomic ratio. The presence of CN amorphous phases was confirmed by the XPS and Raman spectroscopy analysis.

## Acknowledgments

The authors are grateful to Dr Isabel Muñoz Ochando (Instituto de Ciencia y Tecnología de Polímeros ICTP-CSIC) for her assistance in carrying out the Raman spectroscopic analysis. The work was financially supported by Portuguese national funds through the CRUP Institution (project 'Acção N° E – 1007/08) and FCT-Fundação para a Ciência e a Tecnologia, (project PTDC/CTM/102853/2008) and by the Spanish Ministry of Science and Innovation (projects FUNCOAT CSD2008-00023 and MAT2008-06618-C02). REG also wishes to thank the MCINN for the financial support within the Ramón y Cajal programme. This research was partially sponsored by FEDER funds through the program COMPETE-Programa Operacional Factores de Competitividade.

## References

[1] Oliveira C, Escobar Galindo R, Palacio C, Vasquez L, Espinosa A, Almeida B G, Henriques M, Calderon S and Carvalho S 2010 *Thin Solid Films* **518** 5694–9
[2] Mandl S and Rauschenbach B 2002 *Surf. Coat. Tecnol.* **156** 276–81
[3] Oliveira C, Gonçalves L, Almeida B G, Tavares C J, Carvalho S, Vaz F, Escobar Galindo R, Henriques M, Susano M and Oliveira R 2008 *Surf. Coat. Technol.* **203** 490–4
[4] Geetha M, Singh A K, Asokanami R and Gogia A K 2009 *Prog. Mater. Sci.* **54** 397–425
[5] Serro A P, Completo C, Colaço R, Santos F, Lobato da Silva C, Cabral J M S, Araújo H, Pires E and Saramago B 2009 *Surf. Coat. Technol.* **203** 3701–7
[6] Tsai P C, Chen W J, Chen H J and Chang C L 2009 *Thin Solid Films* **517** 5044–9
[7] Musil J and Vlcek J 2001 *Surf. Coat. Technol.* **142–144** 557–66
[8] Mitterer C, Mayrhofer P H and Musil J 2003 *Vacuum* **71** 279–84
[9] Veprek S, Zhang R F, Veprek-Heijman M G J, Sheng S H and Argon A S 2010 *Surf. Coat. Technol.* **204** 1898–906
[10] Musil J 2000 *Surf. Coat. Technol.* **125** 322–30
[11] Martínez-Martínez D, López-Cartes C, Justo A, Fernández A and Sánchez-López J C 2009 *Solid State Sci.* **11** 660–70
[12] Guimarães F *et al* 2008 *Surf. Coat. Technol.* **202** 2403–7
[13] Rai M, Yadav A and Gade A 2009 *Biotechnol. Adv.* **27** 76–83
[14] Duran N, Macarto P D, De Sousa G I H, Alves O L and Esposito E 2007 *J. Biomed. Nanotechnol.* **3** 203–7
[15] Endrino J L, Escobar Galindo R, Zhang H-S, Allen, Gago M R, Espinosa A and Anders A 2008 *Surf. Coat. Tecnoll.* **202** 3675–82
[16] Hlídek P, Hanuš J, Biederman H, Sllavínská D and Pešička J 2008 *Thin Solid Films* **516** 4581–6
[17] Stobie N, Duffy B, McCormack D E, Colreavy J, Hidalgo M, McHale P and Hinder S J 2008 *Biomaterials* **29** 963–9
[18] Arranz A and Palacio C 2002 *J. Phys. Chem.* B **106** 9590–6
[19] Berg S and Nyberg T 2005 *Thin Solid Films* **476** 215–30
[20] Depla D, Buyle G, Haemers J and Gryse R 2006 *Surf. Coat. Technol.* **200** 4329–38
[21] Depla D and Gryse R 2003 *Vacuum* **69** 529–36
[22] Petrov I, Barna P B, Hultmann L and Greene J E 2003 *J. Vac. Sci. Technol.* A **21** S117
[23] Silva E, Rebelo de Figueiredo M, Franz R, Escobar Galindo R, Palacio C, Espinosa A, Calderon S V, Mitterer C and Carvalho S 2010 *Surf. Coat. Technol.* **205** 2134–41
[24] Adamik M, Barna P B and Tomov I 1998 *Thin Solid Films* **317** 64–8
[25] Jung I J and Kang S 2000 *J. Mater. Sci.* **35** 87–90
[26] Dreiling I, Haug A, Holzschuh H and Chassé T 2009 *Surf. Coat. Technol.* **204** 1008–12
[27] Constable C P, Yarwoo J and Munz W D 1999 *Surf. Coat. Technol.* **116–119** 155–9
[28] Robertson J 2002 *Mater. Sci. Eng.* **37** 129–281
[29] Ferrari A C, Rodil S E and Robertson J 2003 *Diamond Relat. Mater.* **12** 905–10